# The Prediction of Permeability for an Epoxy/E-glass Composite Using Optical Coherence Tomographic Images

JOY P. DUNKERS*, FREDERICK R. PHELAN, CARL G. ZIMBA, KATHLEEN M. FLYNN, DANIEL P. SANDERS, RICHARD C. PETERSON, *and* RICHARD S. PARNAS†

*Polymers Division*
*National Institute of Standards and Technology*
*100 Bureau Dr.*
*Gaithersburg, MD 20899*

XINGDE LI *and* JAMES G. FUJIMOTO

*Department of Electrical Engineering*
*Massachusetts Institute of Technology*
*Cambridge, MA 02139*

Knowledge of the permeability tensor in liquid composite molding is important for process optimization. Unfortunately, experimental determination of permeability is difficult and time consuming. Numerical calculation of permeability from a model reinforcement can circumvent experimentation. However, permeability predictions often rely on a model reinforcement that does not accurately mimic the actual microstructure. A rapid, nondestructive technique called optical coherence tomography (OCT) can image the microstructure of a composite in minutes. Actual microstructural information can be then used to improve the accuracy of the model and therefore the predicted permeability. Additionally, the influence on fiber volume fraction and microstructural variability on permeability can be systematically studied.

In this work, binary images were generated from the low contrast OCT data through image de-noising, contrast enhancement and feature recognition. The resulting data were input to a lattice-Boltzmann model for permeability prediction. The influence of the fiber volume fraction, tow surface area, average mean free channel path, and variable microstructure are discussed in terms of their individual and synergistic effects on permeability. The calculated axial and transverse permeabilities from the images show very good agreement with the experimental values.

## INTRODUCTION

Fluid flow in Liquid Composite Molding (LCM) processes such as resin transfer molding (RTM) is usually modeled using Darcy's Law, given by

$$\mathbf{v} = -\frac{\underline{\underline{\boldsymbol{K}}}}{\mu} \cdot \nabla P \qquad (1)$$

where $\mathbf{v}$ is the average (superficial) velocity in the medium, $P$ is the pressure, $\underline{\underline{\boldsymbol{K}}}$ is a symmetric, second order tensor known as the permeability and $\mu$ is the fluid viscosity. Darcy's law is a volume-averaged model in which all the complicated interaction that takes place between the fluid and the fiber preform structure is accounted for through the permeability. Accurate permeability data, therefore, are a critical requirement if *a priori* modeling efforts based on Darcy's law are to be successfully used in the design and optimization of these processes. Currently, the most reliable and commonly used technique for obtaining permeability values is via experimental measurements in

*Corresponding author.
†Present address: Institute of Materials Science, University of Connecticut, Storrs, CT 06269.

either radial or unidirectional flow configurations (1). However, experimental characterization is slow, as it involves a large number of carefully controlled experiments over a large range of volume fractions. Another more serious limitation is that it is difficult to conduct experiments on the materials in the deformed states they encounter when placed in LCM tooling, although there have been some recent efforts (2).

In light of these limitations, computational prediction of permeability (3–7) offers a potentially accurate and robust alternative to experimental methods. Such calculations typically involve imposing a pressure drop across the media, solving the appropriate transport equations for the detailed flow field, and then back-calculating the permeability by applying Darcy's law. The biggest drawback of this approach has been the inability to accurately determine the detailed geometry of the fibrous preform materials, which in addition to many intricate structural features, typically contain statistical variations and defects in their microstructure (8). Without a precise representation of the media, it is not possible to accurately predict permeability values using computational methods.

There have been two main approaches to the problem of microstructure determination. The first is to perform calculations on small, computationally efficient "unit cell" structures using nominal dimensions that represent the average preform weave structure. The major problem with this approach is that calculations on the "average" unit cell structure do not, in general, yield an accurate value for the average permeability (8). A second approach is to determine the microstructure via optical methods (e.g., microscopy), and directly perform the numerical calculation on a discretization of the optical image. This approach has the advantage of accurately representing the media, and by including large sections of the media in the image, variations and defects in the microstructure are automatically accounted for in the calculation. However, until recently, this approach was probably even more tedious to perform than direct experimental measurement of permeability since the composite specimens typically had to be carefully sectioned, polished, and examined. However, a new technique being investigated in this work called optical coherence tomography (OCT) offers a means for rapidly and nondestructively determining the microstructure of fiber reinforced plastic materials, potentially leading to a robust means of computational permeability prediction.

OCT is a noninvasive, noncontact optical imaging technique that allows the visualization of microstructure within scattering media (9–11). OCT uses light in a manner analogous to the way ultrasound imaging uses sound, providing significantly higher spatial resolution (10 to 40 μm) albeit with shallower penetration depth (< 1 cm). This technique is based upon low-coherence optical ranging techniques where the optical distance to individual sites within the sample is determined by the difference in time, relative to a reference light beam, for an incident light beam to penetrate and backscatter within the sample. This temporal delay is probed using a fiber-optic interferometer and a broadband laser light source. The fiber-optic interferometer consists of single-mode optical fiber coupled with a 50/50 fiber-optic splitter that illuminates both the sample and a linearly translating reference mirror. Light reflected from the reference mirror recombines with light backscattered and reflected from the sample at the 50/50 splitter to create a temporal interference pattern, which is measured with a photodiode detector. The resulting interference patterns are present only when the optical path difference of the reference arm matches that of the sample arm to within the coherence length of the source. The axial, or z, spatial resolution that can be obtained with OCT is determined by the coherence length, or inverse spectral width, of the source and is typically (10 to 20) μm (*Fig. 1*). The source is typically a superluminescent diode laser, with a maximum axial resolution of 7 μm. The transverse, or x, spatial resolution of OCT is determined by the focal spot size on the sample which is typically (10 to 40) μm. The ultimate limitation on the depth of penetration within the sample is the attenuation of light caused by scattering. Three-dimensional images of the sample are obtained by rastering the sample in x between successive OCT measurements along the y-axis.

OCT as a nondestructive evaluation (NDE) tool compares very favorably to more established composite NDE techniques. Both transducer and laser based ultrasonics have been used for NDE of polymer composites. Their practical resolution is on the order of 1 mm with tens of mm penetration depth (12, 13). A major drawback to ultrasonics is that the depth of a feature must be determined by model studies, whereas, it is determined straightforwardly using OCT. However, ultrasonic testing can evaluate carbon fiber composites, which absorb too much light to be examined by optical techniques. Both OCT and ultrasonics suffer from contrast degradation and shadowing through the sample thickness. Two X-ray based techniques have been widely used. X-ray radiography is the more established technique, with a spatial resolution of hundreds of micrometers and tens of millimeters in penetration depth (14). The main drawback in performing X-ray radiography is that it results in a two-dimensional representation of three dimensional features. A method more recently applied to composites, X-ray computed tomography (CT), has a resolution similar to OCT and penetration similar to X-ray radiography. Features that do not have a separation, like some cracks, may not be detected. The accuracy of the X-ray attenuation, and thereby the feature intensity and position, is a complex function of many variables, and additional constraints complicate image interpretation (15). However, a great deal of work on image analysis of X-ray tomographic images has resulted in well-established commercial software packages, but the cost of X-ray CT systems is still very high, about

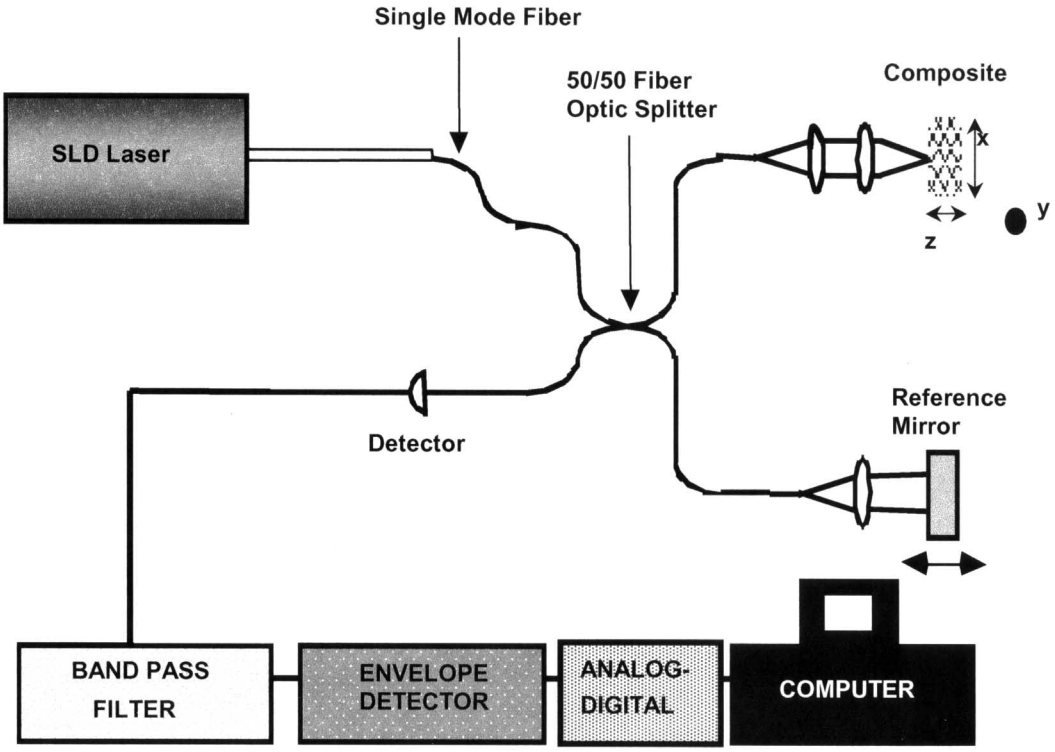


*Fig. 1. Schematic representation of the solid state laser and OCT system layout.*

$300–750k. Nuclear magnetic resonance imaging can reach the spatial resolution of OCT, but is limited to imaging only highly mobile species such as water or plasticizers (16). When considering NDE techniques for microstructure evaluation, a scientist will find that OCT offers an excellent combination of spatial resolution, depth of field, dynamic range, and imaging accuracy.

This work is designed to develop a methodology for calculation of permeability using the actual microstructure of a simple, unidirectional reinforcement from OCT and to examine the strengths and limitations of this approach. The knowledge gained from this work will provide a foundation for investigating the permeability of more complex reinforcement geometries. In addition, the variability of permeability can then be systematically studied as a function of fiber volume fraction and location within a composite.

In this work, volumetric, grayscale OCT images of the microstructure of an epoxy/uni-directional E-glass composite were converted to binary images using custom-written software. Then, these images were input into a 3D flow code based on a lattice-Boltzmann formulation for prediction of axial and transverse permeabilities and compared to experimental values. The predicted permeabilities compare well with the experimental axial and transverse values. The effect of image processing on the computed flow velocity and consequently the permeability is discussed.

## EXPERIMENTAL

### Materials

The epoxy resin systems consisted of a diglycidyl ether of bisphenol A (DGEBA) monomer (Tactix123, Dow Chemical Company, Midland, MI) and two amines (17). Aromatic methylene dianiline (MDA) and aliphatic poly(propylene glycol)bis(2-aminopropyl ether) (JeffamineD400) ($M_n \approx 400$) were purchased and used as received from Aldrich (Minneapolis, MN). The oxirane/amine stoichiometry was 2/1. The amine composition consisted of 0.07 mol MDA and 0.93 mol D400. The refractive index ($n$) of the postcured resin and of the fibers is 1.552 ± 0.004 and 1.554 ± 0.004, respectively, as measured by white light and index matching fluids. The average refractive index of the epoxy composite is calculated by the rule of mixtures for the resin and the fiber volume fraction: $V_{resin} = 0.56$, $V_{fiber} = 0.44$, $(n_{resin})(V_{resin}) + (n_{fiber})(V_{fiber}) = n_{composite} = 1.55$. Therefore, the axial length (z) or depth of field is: 4.5 mm/1.55 = 2.9 mm for each image. Details of the mixing and RTM are provided elsewhere (18).

### Permeability Measurements

A saturated permeability measurement was performed on a unidirectional stitched E-glass preform using axial flow. The fiber preform was created by stacking 8 layers of unidirectional stitched fabric (Knytex D-155, Owens Corning Corp.). Each layer of fabric was offset slightly such that the fiber tows of the preform were in a staggered square array. The

fabric was oriented with the flow direction parallel to the fiber tow direction. The overall dimensions of the preform were 15 cm wide (x), 15 cm long (y), and 1.3 cm thick (z). Several measurements were conducted in a narrow range of fiber volume fractions to obtain a reliable average value as well as error estimates. The model fluid used was a corn syrup solution. The viscosity of the corn syrup solution was measured using a controlled stress rheometer (Bohlin, Visco88). The viscosity was 0.110 Pa·s at 23°C. The flow behavior was Newtonian over the shear rates examined.

The corn syrup solution was injected into the mold under constant pressure conditions. The resin was allowed to flow through the fiber preform until it became fully saturated. After saturation occurred, the volumetric flow rate and mold inlet pressures were measured at several control valve positions. A series of six measurements of the volumetric flow rates and inlet pressures were taken at each valve position over a range of inlet pressures from 0 kPa to 30 kPa. The volumetric flow rate was cycled through this pressure range to ensure that there were no changes in the preform characteristics as a result of the flow. The relative standard uncertainty in the average volumetric flow rate at each control valve position was less than 2% of the average volumetric flow reading. The standard uncertainty in the inlet pressure readings was 0.1 kPa. The permeability was determined from the slope of the linear regression of the volumetric flow rate versus inlet pressure data. The $R^2$ value for the linear regression was 0.99. The resulting axial permeabilities are shown in *Table 1* for similar fiber volume fractions. The average saturated permeability for flow along the fiber tows is $5.3 \times 10^{-6}$ cm$^2$ with an uncertainty of $2.6 \times 10^{-6}$ cm$^2$.

A radial flow experiment was performed for calculation of the transverse permeabilities. The flow anisotropy was found by measuring the ellipticity of the radial flow front (*Table 1*). As expected, the radial flow experiment also indicated that the major axis of the in-plane permeability tensor lies along the tow direction. The transverse permeability was calculated by multiplying the square of the ellipticity by the axial permeability obtained from the saturated flow experiments.

## OCT Instrumentation

The OCT imaging system used in this study is schematically shown in *Fig. 1*. A commercial superluminescent (SLD) light source (AFC Technologies Inc., Hull, Quebec, Canada) is used for the studies reported here. The source operates at 1.3 μm with an output power of up to 15 mW and a spectral bandwidth of 40 nm. The laser light is coupled into a single-mode fiber-optic Michelson interferometer and is delivered to both the reference mirror and the sample. The reference mirror is mounted on a rotating galvanometer, which is driven with a sawtooth voltage waveform. Transverse scanning is performed using a computer controlled motorized stage to translate the sample.

The interferometric signal is electronically filtered with a bandpass centered on the fringe or heterodyne frequency. The filtered fringe waveform is then demodulated, digitized and stored on a computer. The high dynamic range of this system allows back-reflections as weak as a few femtowatts of power to be detected. Images are displayed by mapping the logarithm of the signal strength to a grayscale look-up table. The acquisition time for each image is approximately 1 min. The axial (z) measurement range is determined by the distance the reference mirror moves (4.5 mm) normalized by the refractive index (n) of the sample: 4.5 mm/n. The probe beam is focused to a 30 μm diameter spot at a depth of approximately (750 to 1000) μm below the surface of the sample.

The OCT images are taken for the epoxy composite with the fibers oriented perpendicular to the SLD source. A schematic of the composite orientation with respect to the SLD is shown in *Fig. 2*. In the actual image, the fiber tows are shown as dark gray ellipses and the resin as a featureless light gray region. For any position along the x axis, reflections that represent heterogeneities are collected as a function of z. The sample is then moved with a motorized stage to complete the x, z slice of the composite, and this process is repeated for various positions along the fiber, or y axis. The transverse resolution along the x axis is estimated to be 40 μm. The transverse resolution is governed by spot size and scan rate. There is an inverse relationship between transverse resolution and sampling depth. The axial resolution along the z axis is 20 μm. The distance between slices along the y axis is 50 μm. All original image slices contain 350 × 450 pixels and took about 1 min to acquire. All samples were tilted 4° to avoid collection of the laser reflection from the top surface.

## Image Processing

Before the OCT images can be processed to binary images, an evaluation of how well these images represent the actual composite must be performed. This

**Table 1. Experimental Values of Permeability (K).**

| Percent Fiber Volume | Type of Measurement | K × $10^{-6}$ cm$^2$ | Angle (degrees) | Ratio of ellipse axes |
|---|---|---|---|---|
| 43.8 | Unidirectional, axial, saturated | 1.64 | N/A | N/A |
| 44.2 | Unidirectional, axial, saturated | 7.86 | N/A | N/A |
| 44.4 | Unidirectional, axial, saturated | 5.37 | N/A | N/A |
| 43.8 | Unidirectional, axial, saturated | 6.20 | N/A | N/A |
| 44.2 | Radial unsaturated | N/A | 0 | 0.378 |

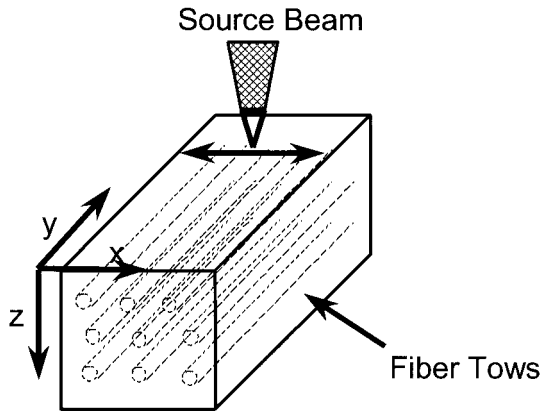


*Fig. 2. Schematic showing the SLD source orientation and sampling directions with respect to the composite.*

will be accomplished by comparing the OCT image with an optical microscopy image of the same sample. However, before that is done, the OCT image must be properly scaled in the axial or thickness direction. The axial distance in the original OCT image must be corrected since there is a temporal delay caused by the fixed arm of the interferometer maintaining a different refractive index than the reference arm, which is moving in air. The distorted image in *Fig. 3a* is the original cross-sectional image referenced to the path of the moving mirror in air.

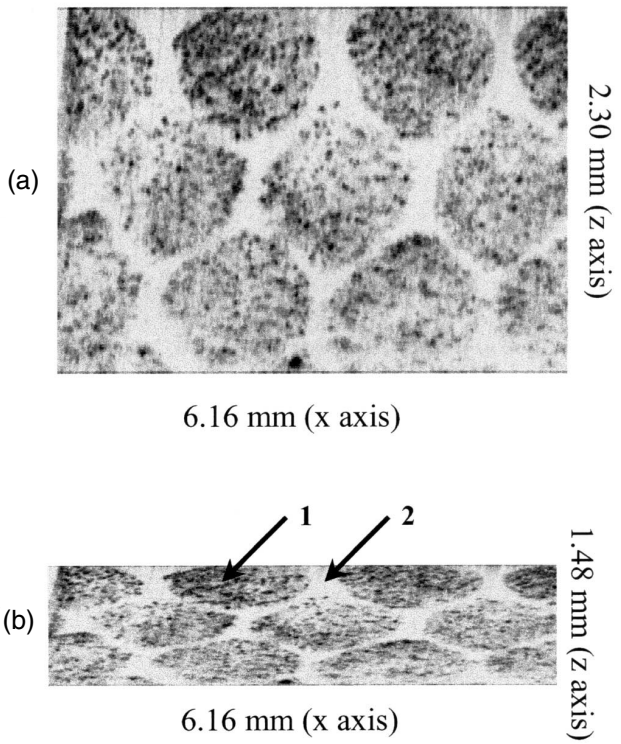


*Fig. 3. As collected OCT cross-sectional image of an epoxy/ unidirectional E-glass composite as referenced to air (A.), Image in A. scaled to the refractive index of the composite (B.).*

The scaling is performed by taking a cross-sectional image of a sample of known thickness. It is critical that the entire thickness of the composite can be clearly seen. In the original image, the distance in the axial direction is known from the pixel resolution and total number of pixels. This distance is divided by the actual thickness of the sample to give the average refractive index of the composite, which is 1.55 in this case. This number is then used in scaling all the images from that particular composite. *Figure 3a* displays an original cross-sectional image of the epoxy/unidirectional composite. *Figure 3b* shows the corrected image. As stated earlier, the dark gray and black ellipses are the fiber tows (Arrow 1) while the resin is the lighter gray region (Arrow 2).

*Figure 4* is a comparison of the optical (a) and an OCT image (b) from this composite. The polished sample end shown in *Fig. 4a* is 5.88 mm in the transverse (x) direction and 1.35 mm in the axial direction (z). *Figure 4b* displays the OCT image of the sample that is 200 μm from the end displayed in *Fig. 4a* that is 6.16 mm in the transverse direction and 1.48 mm in the axial direction. It can be seen by qualitatively comparing *Figs. 4a* and *4b* that the OCT image is an accurate image of the tow size, shape, and placement. The black circles around the tows in *Fig. 4b* are outlines from the corresponding tows in *Fig. 4a* that demonstrate the very good agreement between the optical and OCT images. The fractional area of the tows is 0.77. In the OCT image, some tows seem to have gaps within them that appear as light regions which are not present in the optical image. The presence of the apparent gaps in the OCT images is clearly a drawback, which likely results from loss of contrast and shadowing from highly reflecting features from above. Despite this, the processed OCT images retained their actual shape well since the image processing program focuses on an entire tow. It has been established that OCT can image the microstructure of these epoxy/ unidirectional E-glass composites with good accuracy. The discussion will now focus on the permeability results calculated from the binary OCT images used in the lattice-Boltzmann flow code.

An automated image processing program was written using MATLAB 5.1 with the Image Processing Toolbox to convert the raw grayscale OCT images to binary images of glass fiber and epoxy (*Fig. 5*). The raw image is first rotated and cropped to eliminate sample tilt and edge effects, yielding an image such as in *Fig. 5a*, where the darker ellipses correspond to the three cross-sectional layers of fiber tows while the lighter regions are due to the epoxy. The image is then doubled in size by linear interpolation of adjacent pixels to minimize any artificial alteration of the tow size in subsequent image processing. To increase the contrast between the darker tows and the lighter epoxy regions, a variance image is created replacing the intensity value of a $2 \times 2$ cluster of pixels with the standard deviation of that cluster (*Fig. 5b*). Using the automated program, the boundary of the tows are determined and a binary

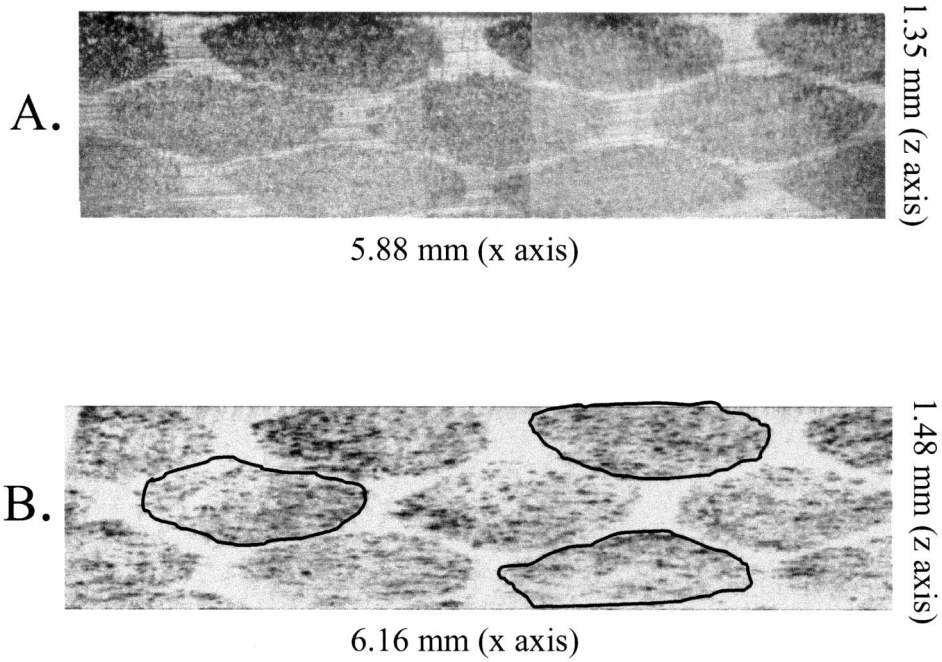


*Fig. 4. Optical microscopy photograph of the sample end (A.), OCT image of the composite in A., 200 μm from the sample end (B.).*

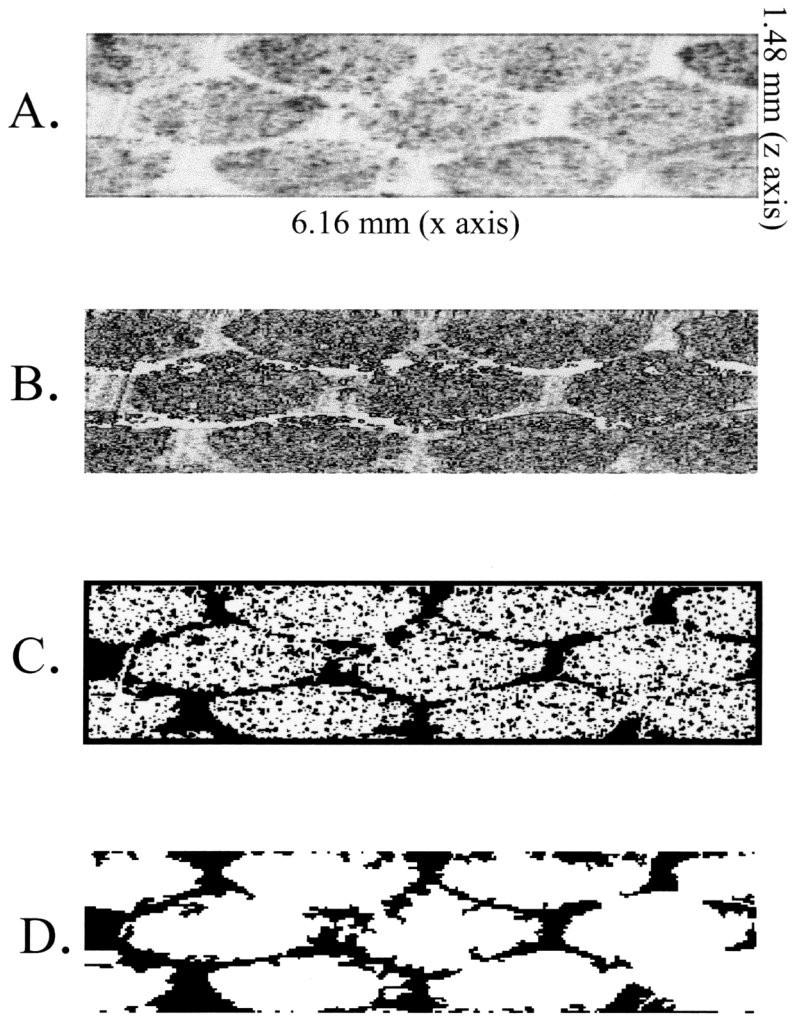


*Fig. 5. Pre-processed OCT image (A.), variance image (B.), binary image (C.), filled final image (D.).*

image (*Fig. 5c*) is formed. In the next two steps, spurious "on" pixels within the image and vertical lines corresponding to detector saturation are eliminated. The image is the scaled to the proper aspect ratio and a filling operation is applied to better define the tows as is seen in *Fig. 5d*. The resulting binary image is then used as input for the permeability calculation. An additional operation may be performed to smooth the rough boundaries of the tows.

## Numerical Simulation

### *Governing Equations*

Modeling the microscale flow in fibrous porous media is complicated by the existence of an open region around the tows, and a porous media inside the tows. Following previous studies, (3–6, 8) the Stokes equation, given by

$$\nabla P = \mu \nabla^2 \boldsymbol{u} \tag{2}$$

is used to model flow in the open regions, and the Brinkman equation, given by

$$\nabla \langle P \rangle = \mu \nabla^2 \langle \boldsymbol{u} \rangle - \mu \underline{\underline{\boldsymbol{K}}}_1^{-1} \cdot \langle \boldsymbol{u} \rangle \tag{3}$$

is used to model flow in the porous regions, where $\underline{\underline{\boldsymbol{K}}}_1$ is the permeability of the porous tows. In both regions, the continuity equation,

$$\nabla \cdot \boldsymbol{u} = 0 \tag{4}$$

is used to model conservation of mass.

### *Lattice-Boltzmann Method*

Solutions to the governing equations above are obtained using a lattice-Boltzmann method described in detail elsewhere (5, 6). In short, the method involves the solution of the discrete Boltzmann equation for the particle velocity distribution function $n_\alpha(\boldsymbol{x}, t)$, where traditional fluid flow quantities such as density and velocity are obtained through the moment sums

$$\rho = m \sum_{\alpha=1}^{N} n_\alpha(\boldsymbol{x}, t) \tag{5}$$

$$\boldsymbol{u} = \frac{m}{\rho(x, t)} \sum_{\alpha=1}^{N} \boldsymbol{v}_\alpha \, n_\alpha(\boldsymbol{x}, t) \tag{6}$$

where $\rho(x, t)$ and $\boldsymbol{u}(x, t)$ are the macroscopic fluid density and velocity, $m$ is the mass of fluid, $\boldsymbol{v}_\alpha$ are components of the discrete velocity space, and $N$ is the number of velocities comprising the velocity space. The particle distribution function $n_\alpha(\boldsymbol{x}, t)$ is governed by the discrete Boltzmann equation given by

$$n_\alpha(\boldsymbol{x} + \boldsymbol{v}_\alpha, t + 1) = n_\alpha(\boldsymbol{x}, t) + \delta_\alpha(\boldsymbol{x}, t) \tag{7}$$

where $\delta_\alpha(\boldsymbol{x}, t)$ is the collision operator which couples the set of velocity states $\boldsymbol{v}_\alpha$. Most LB formulations employ the linear "BGK" form (19–23) of the collision operator in which the distribution function is expanded about its equilibrium value

$$\delta_\alpha(x, t) = -\frac{n_\alpha(\boldsymbol{x}, t) - n_\alpha^{eq}(\boldsymbol{x}, t)}{\tau} \tag{8}$$

where $n_\alpha^{eq}(\boldsymbol{x}, t)$ is called the equilibrium distribution function and $\tau$ is a relaxation time for collisions controlling the rate of approach to equilibrium. The form of the equilibrium distribution function depends on the particular lattice model chosen. The three-dimensional, "d3q15" model (20), which resides on a cubic lattice, is used here (d3 indicates the model is three-dimensional, q15 refers to the number of components in the velocity space). For this model, the equilibrium distribution function is given by

$$n_\alpha = \frac{1}{9}\rho \left(1 + 3\frac{(\boldsymbol{e}_\alpha \cdot \boldsymbol{u}^{eq})}{c} + \frac{9}{2}\frac{(\boldsymbol{e}_\alpha \cdot \boldsymbol{u}^{eq})^2}{c^2} - \frac{3}{2}\frac{(\boldsymbol{u}^{eq} \cdot \boldsymbol{u}^{eq})}{c^2}\right), \alpha = 1,6 \tag{9}$$

$$n_\alpha = \frac{1}{72}\rho \left(1 + 3\frac{(\boldsymbol{e}_\alpha \cdot \boldsymbol{u}^{eq})}{c} + \frac{9}{2}\frac{(\boldsymbol{e}_\alpha \cdot \boldsymbol{u}^{eq})^2}{c^2} - \frac{3}{2}\frac{(\boldsymbol{u}^{eq} \cdot \boldsymbol{u}^{eq})}{c^2}\right), \alpha = 7,14 \tag{10}$$

$$n_{15} = \frac{2}{9}\rho \left(1 - \frac{3}{2}\frac{(\boldsymbol{u}^{eq} \cdot \boldsymbol{u}^{eq})}{c^2}\right) \tag{11}$$

where

$$\boldsymbol{u}^{eq} = \boldsymbol{u} + \frac{\tau \cdot \boldsymbol{F}}{\rho} \tag{12}$$

$\boldsymbol{v}_\alpha = c\boldsymbol{e}_\alpha$, $c$ is the lattice speed, and $\boldsymbol{e}_\alpha$ are the unit vectors along each of the lattice directions in the discrete velocity space, and $\mathbf{F}$ is a body force. To recover the physics associated with the Brinkman equation, the body force

$$\boldsymbol{F} = -s(\boldsymbol{x})\rho \underline{\underline{\boldsymbol{K}}}^{-1} \cdot \boldsymbol{u} \tag{13}$$

is introduced, where $s(\boldsymbol{x})$ is a function equal to 1 in porous media and 0 in open regions. This approach has been validated in previous work.

### *Permeability Computation*

Permeability for different flow directions was computed by imposing a constant pressure along opposite faces of the lattice in the desired direction and integrating the system of equations above to steady-state. The boundary conditions are imposed using the extrapolation scheme of Chen *et al.* (24), and the implementation is described in detail in Spaid and Phelan (6). The boundaries of the flow domain are assumed to be periodic along the faces normal to the flow direction. In all of the simulations, the resolution was 299 × 73 in the x-z plane (as indicated in *Fig. 2*). The depth of resolution in the y-direction is indicated by the number of images in *Table 2*. Estimates for the intra-tow permeability values were obtained from previous work (3). The steady-state velocity field at the inlet was integrated over the surface to obtain the flow rate, $Q$, and this was used in the formula

**Table 2. Experimental and Predicted Values for Axial ($K_{ax}$) and Transverse ($K_{tr}$) Permeability and Brinkman Fraction.**

| Sample Name | Type of Processing | Image Set | Axial $K \times 10^{-4}$ ($mm^2$) | Transverse $K \times 10^{-4}$ ($mm^2$) | Anisotropy Ratio | Brinkman Fraction |
|---|---|---|---|---|---|---|
| Experimental | N/A | N/A | 5.3 ± 2.6 | 0.750 | 7.0 | 0.770 |
| Data 1 | Manual | 87–91 | 4.45 | 0.882 | 5.06 | 0.767 |
| Data 2 | Manual | 75–95 | 3.81 | 0.992 | 4.11 | 0.788 ± 0.021 |
| Data 3 | Automated No Smoothing | 75–95 | 2.83 | 0.654 | 4.32 | 0.768 ± 0.021 |
| Data 4 | Automated Smoothing | 75–95 | 3.18 | 0.991 | 3.21 | 0.750 ± 0.027 |
| Data 5 | Automated Smoothing | 4–24 | 5.09 | 0.934 | 5.45 | 0.727 ± 0.014 |
| Data 6 | Manual Roughened | 75–95 | 2.73 | 0.662 | 4.12 | 0.795 ± 0.021 |
| Data 7 | Manual Dilated | 75–95 | 2.99 | 0.767 | 3.90 | 0.837 ± 0.020 |
| Data 8 | Automated Post-Processed | 75–95 | 3.27 | 0.878 | 3.72 | 0.768 ± 0.014 |

$$K_{eff} = \frac{\mu Q L}{A \Delta P} \tag{14}$$

to obtain the effective permeability, $K_{eff}$, for the desired direction.

## RESULTS AND DISCUSSION

The experimental and calculated axial ($K_{ax}$) and transverse ($K_{tr}$) permeabilities are provided in *Table 2* for comparison. $K_{ax}$ is measured or computed for flow along the fiber tows, or in the y direction as in *Fig. 2*. Image sets for computing K values within this *Table* were processed in two different ways: For the "Manual" method, the tow outlines were drawn by sight and filled in to generate a binary image. Images using the "Automated" method were processed as described in the experimental section. *Figure 6* displays image number 75 from select data sets for visual comparison. For Data 2 (*Fig. 6A*), the $K_{ax}$ of $3.81 \times 10^{-4}$ $mm^2$ is considered to be the best possible value because the images are manually drawn. Part of the discrepancy between the experimental value for $K_{ax}$ ($K_{tr}$) and the calculated values may also originate from micro-scale variations of permeability within the fabric. The twenty-one images used in these calculations represent only a width of 6.0 mm, a depth of approximately 1.5 mm, and, most important, a length of 1.0 mm. For comparison, the size of the reinforcement used in experimental determination of permeability is 15 cm wide (x), 1.3 cm deep (z) and 15 cm long (y). The effect of micro-scale variation in the permeability can also be illustrated by comparing $K_{ax}$ from Data 1 and Data 2. The K from Data 1 is $4.45 \times 10^{-4}$ $mm^2$ and is calculated using five images (y = 0.25 mm), whereas the K from Data 2 is $3.81 \times 10^{-4}$ $mm^2$ and is calculated using twenty-one images (y = 1.05 mm).

The Brinkman fraction (*Table 2*) is defined as the area occupied by the tows and varies slightly from image to image. The average Brinkman fraction is shown along with the standard deviation of the image set. The higher the area occupied by the tows (or the higher the Brinkman fraction), the lower $K_{ax}$ and $K_{tr}$ because there is less open space available for fluid

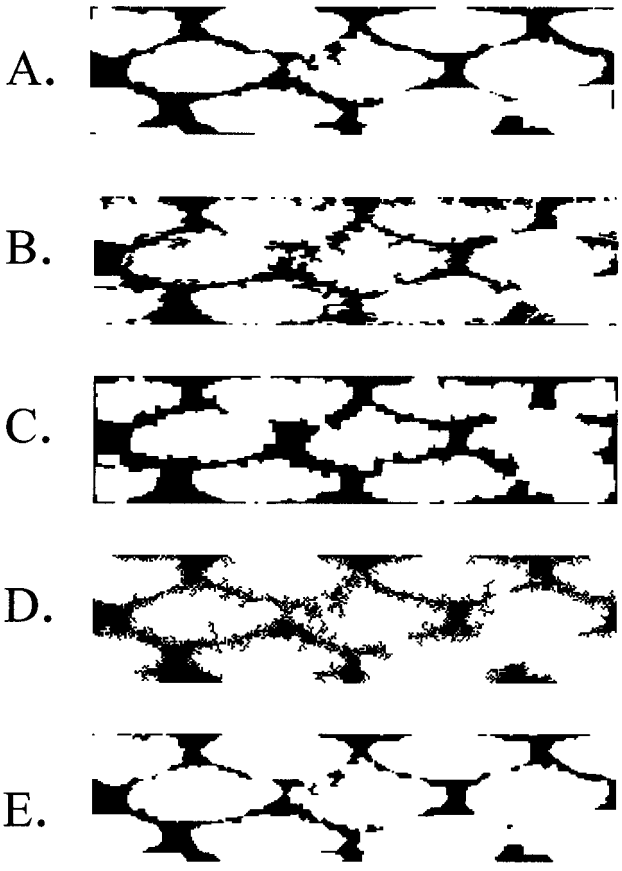


*Fig. 6. Binary images resulting from different image processing techniques. Manually processed image. (A). Automatically processed image (B.), Automatically processed image with smoothing (C.), Manually processed image in A. with added random roughness (D.), Manually processed image in A. with tow dilation (E.).*

flow. If the Brinkman fractions are considered, then the $K_{ax}$ for Data 3 (*Fig. 6B*) should be higher than for Data 2 (*Fig. 6A*) since the Brinkman fraction for Data 3 is slightly lower than for Data 2. For the automatically processed images in Data 3, the $K_{ax}$ is in fact lower than for Data 2. In short, rough tow boundaries are very effective in suppressing fluid velocity and thus artificially decrease permeability. More explanation is provided later in the text. From these results, it is evident that improving the smoothness of the tow boundaries is an important next step.

To improve the smoothness of the tow boundaries, a smoothing operation in the form of a binary opening and closing was performed on the automatically processed data. Data 4 from *Table 2* shows the resulting permeability and Brinkman fraction of the smoothed data. A corresponding image is shown in *Fig. 6C*. Upon smoothing, the permeability increases. However, the resulting Brinkman fraction is substantially lower than for the manually processed images. Thus, this particular smoothing operation is considered to be an unsatisfactory procedure for the image data.

However, comparing the permeability between Data 4 and Data 5 is valid since the same amount of smoothing was applied to each image set. The large difference in permeabilities between Data 4 and Data 5 again illustrates the micro-scale variation of permeability within the reinforcement. Again, both image sets represent a 1.05-mm-long section of sample. Image set 75–95 is 2.55 mm farther down the sample than image set 4–24. Image set 4–24 has three images that contain crossing threads while image set 75–95 has 15 images with crossing threads. These crossing threads are processed into the image as connections between the layers of tows. For the permeability calculation, they are assigned the same intrinsic permeability as the glass tows and also act to suppress the fluid flow. It has been shown experimentally that crossing threads have a large influence on decreasing the permeability and that removal of the crossing threads led to as much as a factor of six increase in the experimentally determined permeability when the same fiber volume fractions and packing geometries were compared (25).

The effect of tow roughness on permeability is illustrated when the permeability results from Data 6 (*Fig. 6D*) and Data 7 (*Fig. 6E*) are compared. The images from Data 6 (*Fig. 6D*) are originally from Data 2 (*Fig. 6A*), the manually processed images. However, a small amount of random roughness was introduced in Data 6 while retaining nominally the same Brinkman fraction, leading to an increase in tow surface area. For Data 7, the images in Data 2 were dilated to increase the Brinkman fraction, but the roughness was not altered. When the axial K from Data 7 is compared to Data 6, the result is initially unexpected. A relative increase of roughly 4% of the Brinkman fraction in Data 7 should lead to a decrease in $K_{ax}$ over Data 6, but the result is the opposite. The $K_{ax}$ of Data 7 is higher than Data 6. This comparison between the permeabilities from Data 6 and Data 7 means that surface roughness is comparable to or more influential than Brinkman fraction in influencing permeability when changes of similar magnitude are compared.

The measure of tow roughness used in this work is the tow surface area. A relative surface area was calculated for each image in the data set by applying an edge detection algorithm in MATLAB that retained only the edge pixels as "on" pixels. Then, the number of these "on" pixels was computed and normalized to the total number of pixels in the image. This number is called the relative surface area. *Table 3* shows the relative surface areas computed for Data sets 2, 3, 6, and 7. The surface area to which the other data is compared is from the manually processed images of Data 2 and is $6.2 \pm 0.4$, where 0.4 is the standard deviation. Note that for the automatically processed images in Data 3, the relative surface area is 2.1% higher than for Data 2. Of greater interest is the surface area of the roughened manually processed tows (Data 6) which is 2.4% higher than for Data 2. For the dilated tows in Data 7, the surface area is about 0.7% lower than for Data 2 because the dilation increased the connectivity between the tows. From these results, knowledge of the Brinkman fraction and tow surface areas points to both as important contributors to permeability. The relative magnitude of their contributions is not yet known. These results also highlight the importance of processing the images as close to the actual structure as possible.

These conclusions are further illustrated by contour plots of the axial velocities of binary cross-sectional images from the different processing routines and are shown in *Figs. 7* and *8*. All these images were derived from the same original OCT image. Clearly, the ideas presented here are general enough to be applied to any image within the data set. These contour plots are all scaled to the minimum and maximum velocity exhibited in the *Fig. 7A*, and all have the same total number of contours. A number denoting the maximum

**Table 3. Comparison of Relative Surface Area and Average Mean Free Channel Path Length of Selected Data Sets. For the Average Mean Free Channel Path Length: 0 = Minimum Length, 21 = Maximum Length.**

| | Data 2 | Data 3 | Data 6 | Data 7 | Data 8 |
|---|---|---|---|---|---|
| Mean relative surface area (% of total pixels) | $6.2 \pm 0.43$ | $8.3 \pm 0.45$ | $8.6 \pm 0.39$ | $5.6 \pm 0.63$ | $6.8 \pm 0.52$ |
| Average mean free channel length/pixel | 2.66 | 2.35 | — | — | 2.44 |

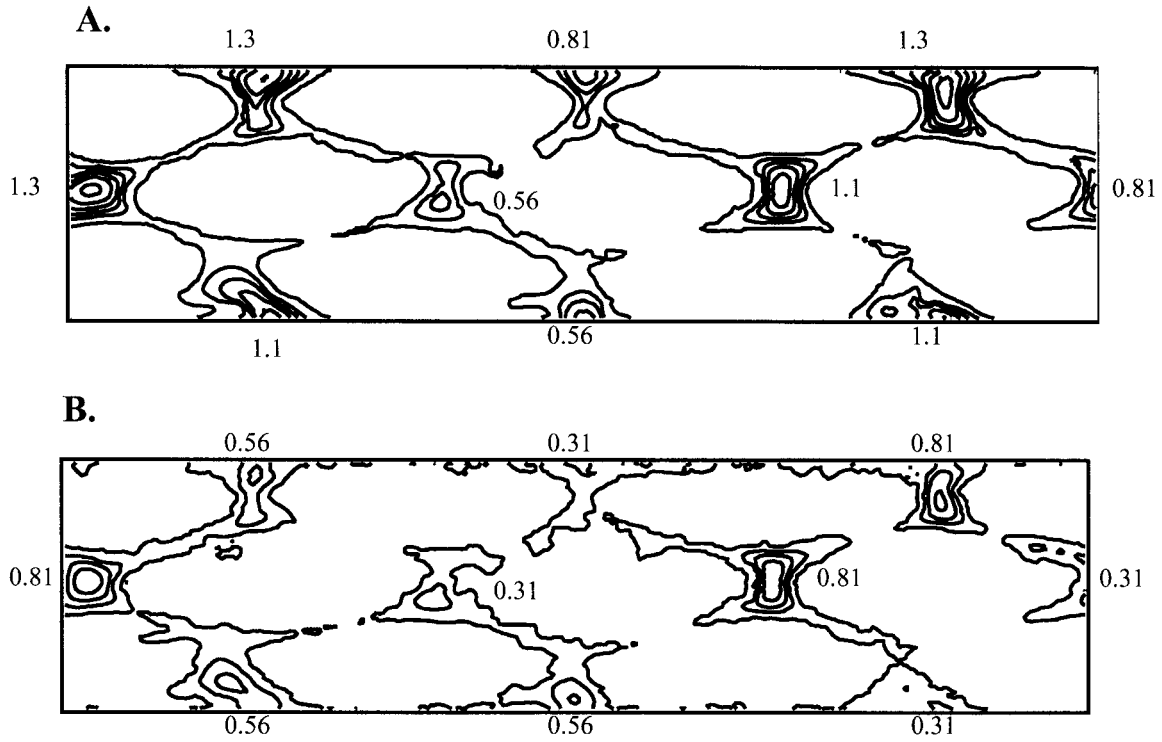


*Fig. 7. Contour fluid velocity plots with maximum channel velocity. Manually processed image. (A.), from Data 2. Automatically processed image (B.), from Data 3.*

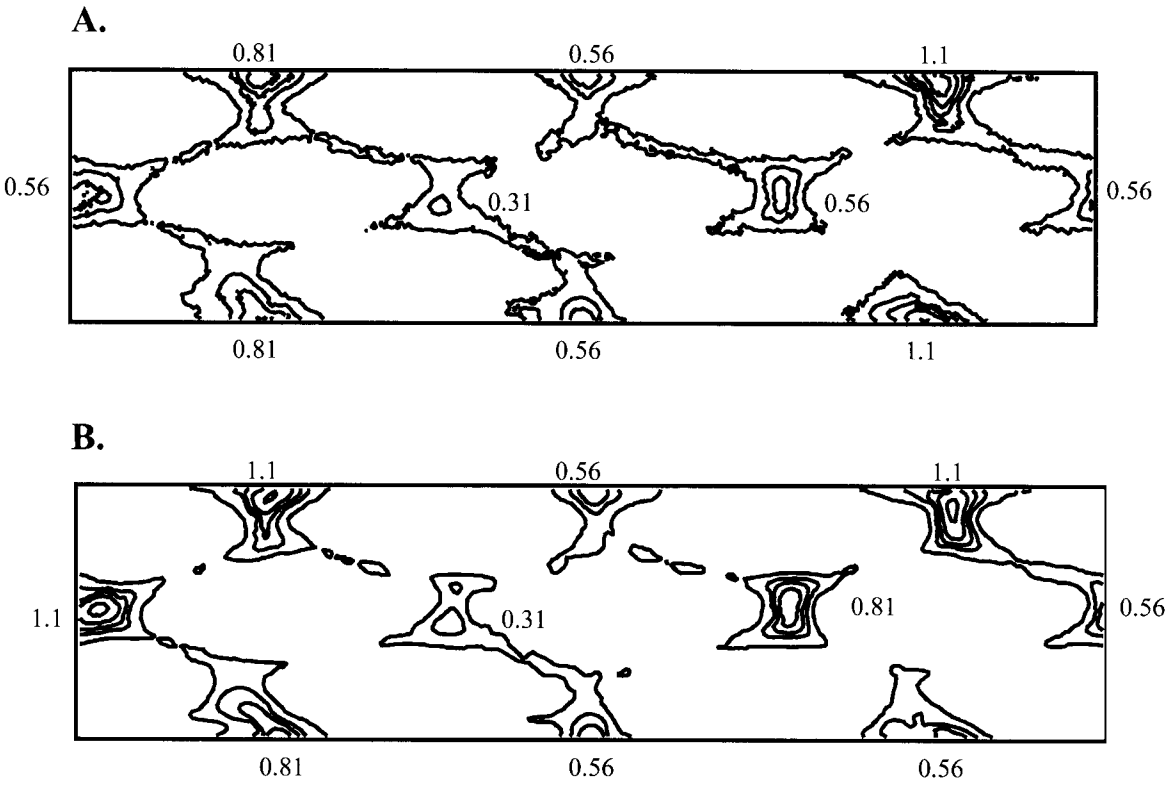


*Fig. 8. Contour fluid velocity plots with maximum channel velocity. Manually processed image in 7A. with added random roughness (A.). Manually processed image in 7A from Data 6, with tow dilation (B.) from Data 7.*

velocity in the channel is provided near the channel. The velocity is the smallest at tow boundary and exhibits a maximum in the center of the channel between the tows.

The images in *Fig. 7* illustrate the influence on the tow boundary roughness on permeability. If *Fig. 7B* is compared to *Fig. 7A*, it is clear that the maximum velocities in the center of the channels is always less than or equal to that in the manually processed images in *Fig. 7A*. This is despite the fact that the Brinkman area of the automatically processed tows is about 3% smaller than for the manually processed tows. If *Fig. 7B* is examined, one can see that overall, the velocity contours are smaller and more irregularly shaped than in *Fig. 7A*. Also, the velocity contours take on the shape of the nearest tow, and this shape influences velocity to the center of the channel where increased resistance to flow occurs from the rough boundary.

More compelling examples are provided in *Figs. 8A* and *8B*. Random roughness was added to *Fig. 8A* that accounted for only a 0.7% increase in the Brinkman fraction relative to the manually processed images (*Fig. 7A*). However, a 30% decrease in permeability resulted from the small scale roughness present in *Fig. 8A* that caused irregularities in the shape of the velocity contours and suppression of flow. The decrease in permeability when the tows are dilated as in *Fig. 8B* when compared to *7A* is caused by simply a decrease in channel radius available for flow. The velocity maximum decreases while shape of the velocity contours is retained.

In order to preserve the Brinkman fraction while minimizing tow roughness, the automatically processed images were subjected further post-processing routine, which eliminates small "peninsulas" emanating from the surface of the tows and then fills in the remaining small "inlets" on the tow surface. A representative post-processed image is shown in *Fig. 9A* along with the corresponding manually (*Fig. 9B*) and automatically (*Fig. 9C*) processed images. *Figure 9A* is derived from *Fig. 9C* through the post-processing routine, but obtains much of the smoothness and Brinkman fraction as *Fig. 9B*. The relative surface area of the resulting data, Data 8, is markedly closer to the surface area of the manually processed image (Data 2) as shown in *Table 3*.

The previous discussion has shown the influence of the free channel radius. However, the free channel path length [i.e. the number of image slices a fluid element can travel along one pixel in the y-direction (parallel to the tow direction) before hitting an obstruction] also influences permeability. This concept is similar to the capillary tortuosity that was discussed in previous work that described the reinforcement in terms of fractals (7). The exact distribution of free path lengths can be calculated using a simple computer program. For each pixel, a mean free path length (average of all free path segments encountered moving in the y-direction along one pixel) is calculated. Since

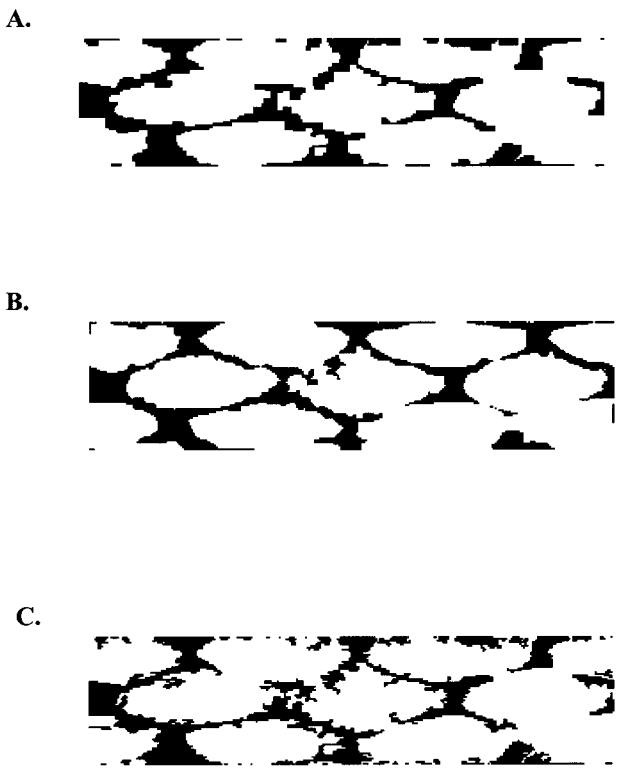


*Fig. 9. Binary images resulting from different image processing techniques. Post-processed image (A.), Manually processed image (B.), Automatically processed image (C.).*

21 images slices were used in the calculation, a value of zero indicates no free path length (i.e. a tow is present) while 21 indicates an unobstructed path. The averages of all the mean free path length per pixel values are shown in *Table 3*. These values do give an indication of the amount of obstruction presented by the reconstructed tows, but do not necessarily give an indication of free channel radii or connectedness of the free channels in the xz-plane. However, the values of average mean free path length per pixel do correlate monotonically with the calculated permeabilities. The average mean free path length of the post-processed images (Data 8) is an intermediate value between the automatically (Data 3) and the manually (Data 2) processed images. The higher value for Data 8 relative to Data 3 despite the similar Brinkman fractions is a result of the smoother tow boundaries. The fluid travels a less tortuous path near the tows for images in Data 8, which, in conjunction with a slightly larger free channel radius, enables a higher fluid velocity maximum than for Data 3. The resulting axial and transverse permeabilities are higher than for the original processing program, and are in excellent agreement with the range of expected values from our experiment. In addition, this post-processing routine is completely automated, allowing for the tows to be reconstructed more rapidly than the manual technique without the influence of human bias.

## CONCLUSIONS

The microstructure of a unidirectional glass-reinforced composite was accurately and rapidly obtained using optical coherence tomography. OCT images were processed and input into a microscale flow model for permeability prediction. It was found that the Brinkman fraction, the tow surface area, and the average mean free channel path generated by the image processing have an important influence on the accuracy of the permeability calculations when compared to the expected values. By optimizing these effects during image processing, excellent agreement between the calculated and the experimental axial and transverse permeabilities was obtained. However, only a small portion of the composite was sampled. The variability of the permeability throughout the composite still needs to be evaluated on many samples. Only by doing this can a true comparison between the experimental and predicted results be performed.

A number of enhancements to this methodology will be implemented for future work on more complex reinforcements. First, images of the entire cross-section of the composite are already being obtained with improved OCT instrumentation. Second, a more robust image processing method based on image gradients to smooth and recognize features will be implemented for the more complex, three-dimensional reinforcements.

## ACKNOWLEDGMENT

This work was supported in part by a grant from the U.S. Department of Commerce, contract 70NANB6H0092. We gratefully acknowledge technical contributions of Dr. Juergen Herrmann, Dr. Wolfgang Drexler, and Mr. Rohit Prasankumar.

## REFERENCES

1. R. Parnas and A. Salem, *Polymer Composites*, **14**, 383 (1993).
2. H. Friedman, R. Johnson, B. Miller, D. Salem, and R. Parnas, *Polymer Composites*, **18**, 663 (1997).
3. S. Ranganathan, G. Wise, F. Phelan Jr., R. Parnas, and S. Advani, *Proc. ACCE94*, 309 (1994).
4. F. Phelan Jr. and G. Wise, *Composites: Part A*, **27A(1)**, 25 (1996).
5. M. Spaid and F. Phelan Jr., *Phys. Fluids*, **9(9)**, 2468 (1997).
6. M. Spaid and F. Phelan Jr., *Composites: Part A*, **29**, 749 (1998).
7. R. Pitchumani and B. Ramakrishnan, *Int. J. Heat Mass Transfer*, **42(12)**, 2219 (1999).
8. S. Ranganathan, R. Easterling, S. Advani, and F. Phelan Jr., *Polymers & Polymer Composites*, **6(2)**, 63 (1998).
9. D. Huang, E. Swanson, C. Lin, J. Schuman, W. Stinson, W. Chang, M. Hee, T. Flotte, K. Gregory, C. Puliafito, and J. Fujimoto, *Science*, **254**, 1178 (1991).
10. J. Fujimoto, M. Brezinski, G. Tearney, S. Boppart, B. Bouma, M. Hee, J. Southern, and E. Swanson, *Nature Medicine*, **1**, 970 (1995).
11. M. Bashkansky, M. Duncan, M. Kahn, D. Lewis, and J. Reintjes, *Opt. Lett.*, **22**, 61 (1997).
12. S. Wooh and I. Daniel, *Materials Evaluation*, **48(5)**, 1206 (1994).
13. R. Dewhurst, R. He, and Q. Shan, *Materials Evaluation*, **51(8)**, 935 (1993).
14. A. Highsmith and S. Keshav, *J. Comp. Tech. Res.*, **19(1)**, 10 (1997).
15. R. Bossi and G. Georgeson, *Materials Evaluation*, **53(10)**, 1198 (1995).
16. P. Jezzard, C. Wiggins, T. Carpenter, L. Hall, J. Barnes, P. Jackson, and N. Clayden, *J. Mat. Sci.*, **27(23)**, 6365 (1992).
17. Identification of a commercial product is made only to facilitate experimental reproducibility and to adequately describe experimental procedure. In no case does it imply endorsement by NIST or imply that it is necessarily the best product for the experimental procedure.
18. J. Dunkers, R. Parnas, C. Zimba, R. Peterson, K. Flynn, J. Fujimoto, and B. Bouma, *Composites, Part A*, **39**, 139 (1999).
19. S. Chen, H. Chen, D. Martinez, and W. H. Matthaeus, *Phys Rev. Lett.*, **67**, 3776 (1991).
20. Y. H. Qian, D. d'Humieres, and P. Lallemand, *Europhys. Lett.*, **17**, 479 (1992).
21. Y. H. Qian and S. A. Orzag, *Europhys. Lett.*, **21**, 255 (1993).
22. P. L. Phatnager, E. P. Gross, and M. Krook, *Phys. Rev.*, **94**, 511 (1954).
23. S. Hou, "Lattice Boltzmann Method for Incompressible, Viscous Flow," *PhD dissertation*, Department of Mechanical Engineering, Kansas State University, Manhattan, Kansas (1995).
24. S. Chen, S. Martinez, and R. Mei, *Phys. Fluids*, **8**, 460 (1996).
25. F. Phelan, Jr., Y. Leung, and R. Parnas, *J. Therm. Comp. Mat.*, **7**, 208 (1994).